

The use of electron optical methods to determine the crystal structure of a modulated phyllosilicate: Parsettensite

R. A. EGGLETON

Department of Geology, Australian National University, Canberra, ACT 2601, Australia

STEPHEN GUGGENHEIM

Department of Geological Sciences, University of Illinois at Chicago, Chicago, Illinois 60680, U.S.A.

ABSTRACT

The crystal structure of parsettensite, approximately $M_{7.5}^+(\text{Mn,Mg})_{49}(\text{Si}_{64.5},\text{Al}_{7.5})_{\Sigma=72}\text{O}_{168}(\text{OH})_{50}\cdot n\text{H}_2\text{O}$ where M^+ is an exchangeable cation such as K, Na, or Ca, was solved by trial-and-error methods based on high-resolution transmission electron microscopy images and electron diffraction data. A simple tilting experiment was utilized to determine qualitatively the magnitude of dynamical diffraction effects for reflections in a diffraction plane. Thus, it was determined that a kinematical approximation could be used, since dynamical diffraction effects were minimized by using very thin grains and superstructure reflections streaked parallel to c^* were not affected significantly by orientation changes near the (001) plane. Derived structural models of a single layer projected down c were compared with hk Fourier transforms. The technique was capable of discriminating among models. A distance least-squares (DLS) refinement confirmed that the tetrahedral linkages are dimensionally reasonable, and DLS-derived atomic coordinates are given. The ideal three-dimensional model conforms to $C2/m$ symmetry with cell parameters, derived from X-ray powder methods, of $a = 39.1(1)$, $b = 22.84(5)$, $c = 17.95(6)$, $d_{001} = 12.56 \text{ \AA}$, and $\beta = 135.6(2)^\circ$.

Parsettensite is a modulated 2:1 layer silicate. It consists of a continuous Mn-rich octahedral sheet coordinated by silicate tetrahedral rings forming islands three tetrahedral rings wide. Pairs of islands are linked by inverted and partially tilted tetrahedra that form four-membered ring interisland connectors, with junctions of three islands forming also 12-membered ring connectors. Layers are cross-linked through two sets of four-membered ring connectors (double four-membered rings). Although the tetrahedral island connectors are different from those in stilpnomelane, the tetrahedral islands are similar, which explains the similarities in the diffraction patterns of the two minerals, as noted by earlier workers.

INTRODUCTION

Parsettensite is a poorly described Mn-rich hydrous phyllosilicate with d_{001} equal to about 12.6 Å. Müller (1916) first presented physical, chemical, and optical data for this mineral, but it was Jakob (1923, 1933) who apparently named parsettensite and offered detailed chemical and optical data for both parsettensite and "errite." "Errite" was later shown to be a variety of parsettensite with a light green color instead of brown-red (Geiger, 1948), possibly caused by mixed oxidation states of constituent Mn or Fe. Geiger (1948) presented additional analyses and optical information and also provided an X-ray study coupled to dehydration experiments. Geiger reemphasized the possibility that parsettensite is the Mn end-member of stilpnomelane, which was suggested earlier by Hutton (1938) on the basis of chemistry and poor-quality Laue X-ray data.

More recently, Eggleton (1972) argued that the parsettensite analysis of Jakob (1923) does not conform to his proposed structure of stilpnomelane. Subsequently, ab-

stracts published simultaneously by Ozawa et al. (1986) and Guggenheim (1986) showed that parsettensite is distinct from stilpnomelane. Electron diffraction patterns revealing differences between parsettensite and stilpnomelane were published by Guggenheim and Eggleton (1987, 1988) in papers giving the systematics of the modulated 2:1 layer silicates. Guggenheim and Eggleton (1987, 1988) noted also that parsettensite is similar to stilpnomelane in that both structures are modulated 2:1 layer silicates with continuous octahedral sheets and islandlike regions of ideal tetrahedral sheets separated by inverted tetrahedra. The d_{001} value of 12.6 Å suggests that tetrahedra in the interlayer space are joined along c through apical O atoms. Mn-dominant stilpnomelane, however, has been reported (Dunn et al., 1984, 1992), although the amount of Mn does not greatly exceed about half of the possible octahedral sites in the stilpnomelane structure.

Ozawa et al. (1986) reported that parsettensite has an orthohexagonal-based cell with $a = \sqrt{3}b = 39.1$, $b = 22.6$, and $d_{001} = 12.6 \text{ \AA}$, and they suggested that the true symmetry is probably monoclinic. A prominent pseu-

dotrigoal cell was reported also, with $a_1 = a_2 = 22.6 \text{ \AA}$ parallel to the orthohexagonal **b**. From the $hk0$ net, a sublattice was defined on the basis of the trigonal cell, with $a_1/7$ and $a_2/7$, and the superstructure contains the ratio of 72 Si atoms to 49 octahedral atoms. Ozawa et al. noted also considerable stacking disorder. Guggenheim and Eggleton (1988, p. 723) presented an indexed powder pattern based on lattice parameters of $a = 39.47$, $b = 22.78$, $c = 14.63 \text{ \AA}$, $\beta = 120.8^\circ$.

Parsettensite occurs at Val d'Err, Oberhalbstein, Graubünden, Switzerland, in metasedimentary manganese ore deposits with manganese silicates and carbonates (Geiger, 1948) under low-grade to very low-grade conditions. Shear zones show evidence of fluid circulation, with parsettensite commonly occurring in veins. In addition, similar material obtained for this study occurs near Chiavari and Gambatesa, Italy. An abundant phase (White, 1987) from the Foote mine, Kings Mountain, North Carolina, was subsequently identified as parsettensite (Guggenheim and White, unpublished manuscript). In this occurrence, parsettensite forms "spherical clusters of well-defined platy" crystals (White, 1987) on surfaces of pegmatite, suggesting either a hydrothermal or pneumatalytic origin. Parsettensite was described also by Sameshima and Kawachi (1991), in association with the Mn-rich zussmanite mineral, coombsite, from a Mn-rich siliceous lens in a very low-grade (pumpellyite-prehnite facies) metagraywacke and argillite sequence near Otago, South Island, New Zealand. Sameshima and Kawachi (1991) indexed a cell using a β angle of 95.6° and other cell parameters similar to those of Ozawa et al. (1986).

The purpose of this study is to determine the crystal structure of parsettensite, which has a complex superstructure. Traditional structural analysis, however, is not possible because samples are fine-grained and impure. In addition, extensive stacking disorder makes the use of certain powder methods, such as the Rietveld method, inadvisable. Therefore, high-resolution transmission electron microscopy (TEM) is used, along with other powder X-ray diffraction techniques.

It is generally recognized that electron dynamical diffraction effects preclude the possibility of obtaining useful electron diffraction data for Fourier analysis, although work by Soviet researchers using only kinematical approximations (for a summary, see Drits, 1987) appeared successful for structural refinement procedures. We show in this study a rapid procedure to determine experimentally if dynamical effects are insignificant, so that a structural determination can proceed using kinematical approximations. Furthermore, we show that rudimentary measurements of electron diffraction intensities can be used successfully to test structural models derived from trial-and-error approaches and Fourier methods. Although the method is applied to a modulated phyllosilicate, similar procedures may be useful for other materials, especially where there are weak superlattice reflections originating from small perturbations of the cell involving atoms with a low atomic number.

Because we combine multiple procedures to solve a very complex structure, it is important to understand that the goal of this study is to outline the structure of parsettensite. Data were not of sufficient quality to refine the structure. After obtaining chemical data, we proceeded with a one-dimensional powder X-ray study to provide initial information about the interlayer connectors. Such information was enhanced by examining Cs-exchanged material also. This information and the electron diffraction and high-resolution TEM images allowed the development of several models. These models were tested against limited electron diffraction data by using Fourier techniques. The best model, which consisted of crudely determined atomic coordinates, was refined using distance least-squares (DLS) techniques. This technique uses the topology of the proposed structure and adjusts atomic coordinates on the basis of assigned weighted interatomic distances; the procedure did not involve any data from parsettensite directly. The purpose of this step was to check that the topology was reasonable and to obtain more realistic atomic coordinates for further testing of the best model. Using these coordinates, we calculated high-resolution TEM images and compared them in detail to the observed images. A companion paper (Guggenheim and Eggleton, 1994) provides further DLS calculations for parsettensite and stilpnomelane, since both structures appear to be related.

CHEMICAL ANALYSIS

Samples were analyzed (Table 1) using a JEOL JSM-6400 scanning electron microscope (SEM) with an energy-dispersive spectrometer (EDS). Operating conditions included a 15-kV beam, a 40° take-off angle to the Si(Li) detector, and a 90° incidence angle to the sample. A $20\text{-}\mu\text{m}$ square raster was used with a 1-nA beam current. Unlike samples with volatiles and some other cations where heating by the electron beam produces a loss of elemental concentration, a single spot beam showed increasing K concentrations with time, indicating K movement toward the beam. This is also consistent with the behavior of stilpnomelane. With further analysis on a single spot, a loss of Si, Al, and Mn occurred. The rapid deterioration of the sample using a single spot analysis or raster mode at sufficient beam current precluded the accurate use of a wavelength-dispersive spectrometer (WDS).

Table 1 presents calculated formulae on the basis of 72 tetrahedral sites. All samples show a significant presence of Al, assigned to the tetrahedral sites according to the rationale given by Guggenheim and Eggleton (1987, p. 733). Also noteworthy is the significant amount of K and Ca, which probably occupy sites in the interlayer region along with H_2O . A wet-chemical analysis averaged from three analyses of material from Val d'Err (Jakob, 1933) is given for comparison. The wet-chemical analysis by Geiger (1948) for this sample is omitted because of its unusually high CaO (5.74 wt%), presumably from calcite contamination.

TABLE 1. Chemical analyses of parsettensite

	Val d'Err		Gambatesa	
	1	2	3	4
SiO ₂	45.95 ± 0.28	43.02	43.79 ± 0.27	44.99 ± 0.28
Al ₂ O ₃	4.97 ± 0.16	4.19	4.05 ± 0.16	4.51 ± 0.16
TiO	<0.14 ± 0.07	0.01	<0.56 ± 0.09	<0.17 ± 0.07
Cr ₂ O ₃	<0.14 ± 0.14		<0.14 ± 0.08	<0.14 ± 0.08
FeO	<0.31 ± 0.20		<0.30 ± 0.20	2.58 ± 0.26
Fe ₂ O ₃		0.51		
MnO	34.67 ± 0.35	35.48	37.77 ± 0.36	35.12 ± 0.35
MgO	2.75 ± 0.14	2.65	0.97 ± 0.11	4.65 ± 0.35
CaO	0.78 ± 0.08	0.24	0.38 ± 0.07	0.34 ± 0.07
Na ₂ O	<0.20 ± 0.12	0.33	<0.20 ± 0.12	0.33 ± 0.13
K ₂ O	2.03 ± 0.08	0.78	2.59 ± 0.09	3.28 ± 0.09
H ₂ O ⁺		9.01		
H ₂ O ⁻		3.85		
Total	91.32	100.07	90.12	92.23
		Based on 72 tetrahedral cations		
Si	63.86	64.59	64.92	64.39
Al	8.14	7.41	7.08	7.61
Total	72	72	72	72
Ti	0.00	0.01	0.62	0.18
Fe	0.00	0.58	0.00	3.09
Mn	40.81	45.12	47.43	42.58
Mg	5.70	5.93	2.14	1.92
Total	46.51	51.64	49.58	47.65
Ca	1.16	0.39	0.60	0.52
Na	0.00	0.96	0.00	0.92
K	3.60	1.49	4.90	5.99
Total	4.76	2.84	5.50	7.43
H	80*	90	98*	74*

Note: 1 = From Val d'Err, Oberhalbstein, Graubünden, Switzerland; EDS analysis of sample from Geiger collection labeled P-24; 2 = wet-chemical analysis based on the average of three samples from Jakob (1933), from Val d'Err, Oberhalbstein, Graubünden, Switzerland; 3 = labeled as Harvard no. 92661 from Gambatesa, Italy; 4 = from Gambatesa mine, Chiavari, near Genoa, Italy.

* Based on difference.

X-RAY AND CATION-EXCHANGE STUDY

One-dimensional electron-density projection

One-dimensional electron-density projections derived from oriented powder X-ray diffraction methods are useful to provide *z*-coordinate information about atomic planes in the 2:1 layer and information about the nature of the material in the interlayer. The technique is especially useful for materials that show cation-exchange capabilities, such as parsettensite.

Parsettensite from Gambatesa mine, Chiavari, Italy, was abraded with an Fe file to produce fine-grained material for X-ray study. A slurry of H₂O and sample was prepared and sedimented on a glass plate to produce a sample with grains well oriented on (001). Experiments were made on a Siemens D-501 automated θ : 2θ goniometer using CuK α radiation and a graphite monochromator at 50 kV and 30 mA. Scans were made at intervals of 20–100° 2θ with 1° divergence and scatter slits and at 4–30° 2θ with 0.3° slits. A step-scan mode was employed for both scans at 0.02° intervals, with count times of 4 s per step. The 003 and the 004 peaks are common to both scans and were used to scale peaks below 20° 2θ . Intensity measurements were determined from the peaks after K α_2 stripping and curve smoothing using the Diffrac AT program (Socabim, 9 bis, villa du Bel-Air, 75012 Paris, France). Intensities were corrected for Lorentz-polarization effects.

Initial one-dimensional electron-density maps were calculated by determining the phases based on the *z* coordinates for an ideal 2:1 layer silicate model with Mn in the octahedral sites. Atoms were considered fully ionized, except for O, which was considered half-ionized. The initial assumption was that parsettensite is based on a 2:1 layer silicate, an assumption that is consistent with the electron-diffraction and imaging data (see below). The resultant Fourier map (Fig. 1 top), however, shows significant electron-density in the interlayer region at *z* = 0.385 and at *z* = 0.48–0.50, suggesting that the structure must differ from an ideal 2:1 layer silicate model, which would have either no electron density (e.g., talc) or a considerably different amount at *z* = 0.50 (e.g., mica).

Several maps were calculated by removing material at *z* = 0.202 (Si) that makes up part of the 2:1 layer and adding electrons at *z* = 0.385, which represents Si associated with inverted tetrahedra. In addition, it was found that more scattering material was needed near *z* = 0.5 than could be explained by the apical O atoms of inverted tetrahedra, suggesting the location of K, Ca, and H₂O. Figure 1 (top) shows the resulting direct-Fourier and difference-Fourier maps for the best model based on the nine observed reflections, with an *R* value of 0.042 ($R = \Sigma |(F_o - F_c)| / \Sigma |F_o|$).

The derived one-dimensional structure shows a considerable spread in electron density where, in an ideal phyllosilicate, planes should project to a point. This result

suggests considerable positional disorder within the planes of projection. Positional disorder may be modeled by assigning atoms of one plane a large isotropic temperature factor (B) or by splitting the average plane into several closely spaced planes. For parsettensite, the Mn plane with more efficient scattering ($z = 0.00$) was split into three planes ($z = 0.00, 0.02, \text{ and } 0.04$) with $B = 0.5 \text{ \AA}^2$. In contrast, the scattering efficiency of the O atom is less. Thus, the octahedral anion plane at $z = 0.087$ and the basal anion planes at $z = 0.265, 0.330, \text{ and } 0.380$ have not been split, but atoms have been assigned larger B values of 3.0 \AA^2 . All other planes have atoms assigned B values of 1.0 \AA^2 .

The best fit for electron density is derived with 48 Si ($z = 0.202$) located within the 2:1 layer and 24 Si ($z = 0.385$) inverted relative to the 2:1 layer. There are 72 basal O atoms at $z = 0.265, 24$ at $z = 0.330, \text{ and } 12$ at $z = 0.380$. In addition, there are 11 O equivalents (or, in terms of electron density, $K_{5.5}$) at $z = 0.48$ and 18 O (or 12 apical O atoms + $6\text{H}_2\text{O}$) at $z = 0.50$. The different z coordinates at 0.48 and 0.50 may not be significant. Because the residual R is not sensitive to small differences in scattering and despite the good fit, this model should not be considered a unique solution. In fact, the data are consistent also with the linkage involving four-membered ring tetrahedral connectors as determined by Fourier analysis from the electron diffraction experiments (see below).

Cation-exchange and one-dimensional electron-density projection

Cation exchange experiments were made to test the assumption that K is an exchangeable cation and not an integral part of the structure. Furthermore, by comparing the one-dimensional electron-density maps of the exchanged sample with the original sample, it became possible to locate unambiguously the exchangeable cation sites.

Exchange of K by Cs was obtained by placing the powder used in the X-ray experiments in a 1- N CsCl bath for 48 h at room temperature. The sample was washed twice in distilled H_2O and recovered each time by centrifuging. The H_2O and sample slurry was prepared in a similar manner as above, and the X-ray data were collected and treated in an identical way.

The cesian parsettensite data were modeled from the results of the natural sample, with all parameters fixed except those relating to the interlayer. For the exchanged sample, there are 30 O equivalents (or $\text{Cs}_{5.0}$) at $z = 0.48$ and 18 O (or 12 apical O atoms + $6\text{H}_2\text{O}$, if it is assumed that there are $6\text{H}_2\text{O}$ present) at $z = 0.5$. The R value is 0.070.

ELECTRON-OPTICAL STUDY

Parsettensite samples were studied by transmission electron microscopy on a JEOL 100CX and a JEOL 200CX instrument. The JEOL 100CX allows a large de-

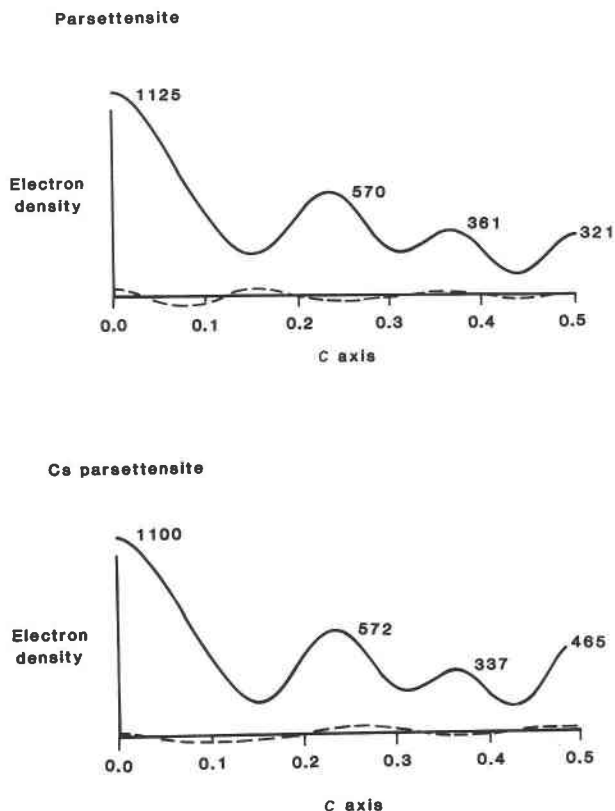


Fig. 1. One-dimension electron-density projection of parsettensite, Chiavari, Italy (top) and of the same material after Cs exchange (bottom). Solid curve is electron density, and dashed curve is the electron difference between observed and calculated values. Values near the peaks indicate number of electrons. See text for details.

gree of tilt ($\pm 60^\circ$), either by using a tilt-rotate or a double-tilt stage. Hence, a large portion of the reciprocal lattice can be studied, and it is possible to constrain the development of a model by defining the unit cell and symmetry. In contrast, the JEOL 200CX has a more restricted sample-tilt capability ($\pm 10^\circ$), with a double-tilt stage, but offers better resolution. The greater resolution provides crucial structural information. In addition, a model may be used to calculate images for comparison with the observed images from the 200CX as a test to help confirm the correctness of the model.

Samples were prepared for TEM study in two ways. Ar ion-thinning techniques were used in conventional ways to produce samples used for both instruments. In addition, samples were prepared for lattice orientation studies near the basal plane by abrading parsettensite with an Fe file and dispersing the particles in an alcohol bath with an ultrasonic vibrator. A drop of this alcohol bath was placed on a holey carbon grid and allowed to evaporate. Because of the perfect (001) cleavage of parsettensite, the resulting sample for examination contained primarily particles oriented on the basal plane.

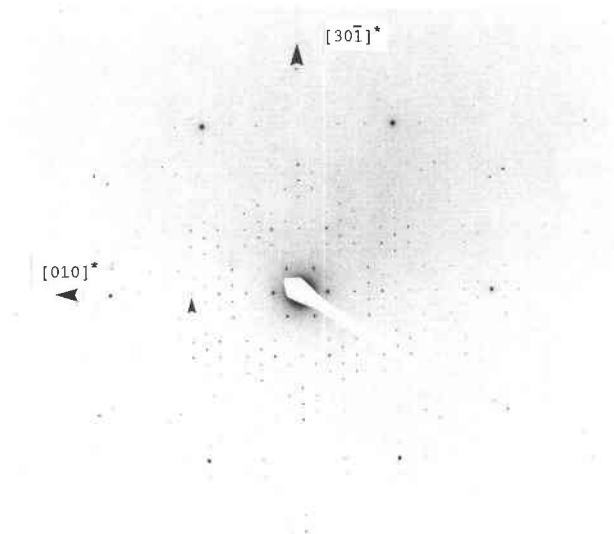


Fig. 2. Selected-area electron diffraction pattern of parsettenite, Gambatesa, Italy, along c^* . This approximately represents the basal plane, near the a and b axes. The direction labeled $[30\bar{1}]^*$ is along a (compare with Fig. 4). The arrowhead points to the 08 reflection and represents one point of a six-pointed star, as discussed in the text.

Diffraction data

The diffraction pattern obtained for flakes on the (001) plane (basal plane net) was used extensively for modeling purposes. For a β angle of near 135° (see below), the normal to this plane is $[103]$. A notable feature of the electron diffraction pattern (Fig. 2) is the strong 0,14 reflection and its pseudosymmetry equivalents, which produce a hexagon on the net. In an ideal 2:1 layer silicate without a superstructure, this reflection corresponds to the 06 reflection.

Another major feature of this two-dimensional net is the overall intensity distribution, which resembles a six-pointed star with the 08, 12,4 (i.e., $h = 12$, $k = 4$), and $12,\bar{4}$ as points of the star, based on the parsettenite superstructure. An arrowhead shows the 08 reflection in Figure 2, and the other points are at 60° intervals in the net. Minor features, but important for purposes of modeling, are the strong 02, 31, and 91 reflections.

A small rotation of approximately 5° about $[100]$ produces a major change in intensity for only the strong subcell reflections. These reflections arise from a substructure attributed to the Mn octahedral sheet. In contrast, the superstructure reflections caused by the tetrahedral sheet remain similar in intensity upon specimen rotation. In fact, large rotations of up to $\pm 50^\circ$ away from the basal plane net do not significantly affect the relative intensities of the superstructure reflections.

The $Ok\bar{l}$ net (Fig. 3) is characterized by rows of $k = 14n$ and $k = 14n \pm 2$ that have sharp reflections. These reflections fall on reciprocal lattice nodes that correspond

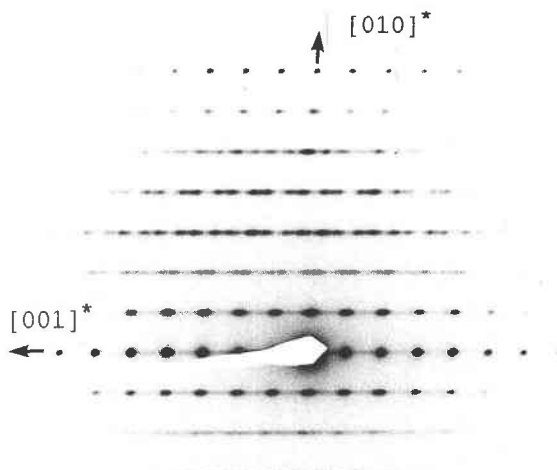


Fig. 3. The $Ok\bar{l}$ net shows rows of sharp reflections at $k = 14n$ and $k = 14n \pm 2$. Systematic absences conform to a C -centered cell, with $k = 2n$ reflections present. Note that most rows have reflections that are streaked and quasi-periodic along c^* . The sample is from Gambatesa, Italy.

to an α angle of 90° . In contrast, rows $k = 14n \pm 4$ or $6, 8, 10$ do not maintain periodicity along c^* , and more intense streaking is common.

The $h0l$ net (Fig. 4) has a sinusoidal variation in intensity perpendicular to the c^* axis, with stronger maxima along $h = 14n$ rows. Essentially untwinned crystals, as illustrated in Figure 4, are extremely rare, even when the smallest aperture is used in the selected-area diffraction mode and hundreds of crystals are examined. The choice of the β^* angle of either approximately 44° or 60° may be made. Although 60° was used previously by Guggenheim and Eggleton (1988, p. 723), β^* of 44° was chosen in this study for convenience of modeling. A β^* of 84.4° to produce a β angle of 95.6° , as suggested by Sameshima and Kawachi (1991), is not possible. All nets (see Figs. 2–4) are consistent with a monoclinic-shaped cell and C centering. Thus, the space group symmetry is most likely $C2/m$, $C2$, or Cm . Table 2 presents an X-ray powder pattern (Guggenheim and Eggleton, 1988, p. 723) indexed with the derived unit-cell parameters in space group $C2/m$. The importance of the powder pattern is that it provides high accuracy for the unit-cell parameters. In contrast, small tilt errors for the principal planes in electron-diffraction reciprocal space can adversely affect the measured interaxial angles.

Comparison of Figures 2 and 4 shows that the basal plane net (Fig. 2) is not ideal because it is complicated by extra reflections, caused by streaking along c^* , which is produced by stacking disorder. Because there is no variation in intensity as the specimen is tilted away from the basal plane, the stacking disorder is complete. Consequently, Figure 2 is interpreted as arising from a single layer, thereby allowing the use of Fourier synthesis. Thus, the basal plane net is treated as an hk net. For example,

TABLE 2. X-ray powder pattern of parsettensite

<i>hkl</i>	<i>l</i>	<i>d</i> _{obs}	<i>d</i> _{calc}	<i>hkl</i>	<i>l</i>	<i>d</i> _{obs}	<i>d</i> _{calc}			
001	200	12.62	12.57	532			2.920			
020	40	11.37	11.42	153	20	2.923	2.903			
31 $\bar{1}$			11.33	772			2.812			
22 $\bar{1}$			9.52	570			2.804			
40 $\bar{1}$	25	9.62	9.51	773	70	2.791	2.784			
220			8.77	14,0,4			2.772			
402			8.62	771			2.707			
111	15b	8.62	8.54	282	20	2.708	2.705			
130			7.34	14,0,3			2.637			
42 $\bar{1}$			7.31	774			2.632			
002	30	6.27	6.29	682	100	2.639	2.616			
150	50	4.51	4.51	372	20	2.512	2.531			
732			4.48	005			2.514			
35 $\bar{1}$			4.31	770			2.507			
642	30	4.28	4.30	14,0,7	15	2.464	2.463			
913			4.27	883			2.459			
003			4.191	14,0,2			2.424			
624	50	4.195	4.176	775	60	2.417	2.409			
151			4.092	14,0,1			2.186			
152			3.885	776			2.168			
734	25b	3.780	3.844	0,14,0	70	1.628	1.632			
113			3.711	7,7,4			1.630			
204			3.691	21,7,7			1.618			
004	40	3.145	3.143	0,14,1	45	1.615	1.618			
572	15	3.006	3.001	14,0,2	35	1.575	1.576			
							008	1	1.570	1.571
							0,14,3	20	1.516	1.520

Note: *b* = broad; *a* = 39.1(1), *b* = 22.84(5), *c* = 17.96(6) Å, β = 135.6(2)°. Data from Guggenheim and Eggleton (1988); Debye-Scherrer photograph by I. Threadgold and supplemented by 00*l* diffractometer data.

an alternative index for 60 $\bar{2}$ assuming completely random stacking along *c*, is the 60, and the layer lines, as counted from the origin along this direction, can be indexed as 1*k*, 2*k*, 3*k*, etc.

The degree of streaking along *c** is usually high and often varies among crystals. Most crystals show twinning such that streaking may occur between reciprocal lattice nodes representing different twin components. This suggests that twinning is related to translations between adjacent layers and thus involves stacking faults.

High-resolution TEM images

The most informative high-resolution TEM image is that from the *h0l* net (Fig. 5). Because of the large size of the unit cell, other crystallographic directions do not provide useful information. Figure 5 was produced by allowing all reflections within the radius of 0.5 Å⁻¹ to pass through the objective aperture of the JEOL 200CX. The image shows a row along (001) of elongated maxima (with the elongations nearly perpendicular to [100]) with the maxima separated at intervals ranging from 2.5 to 3.1 Å. Such intervals, which are not well resolved, may be related to the dominance of reflections with 39.1-Å/14 = 2.8-Å spacings, deviations from focus, or changes in thickness. Between these rows of maxima, regions of high electron density (forming what appears as pillars) approximately 4.6 Å in width alternate with areas of little or no electron density, approximately 3.5 Å in width. There are two types of high-density regions or pillars, with one pillar of greater electron density alternating with

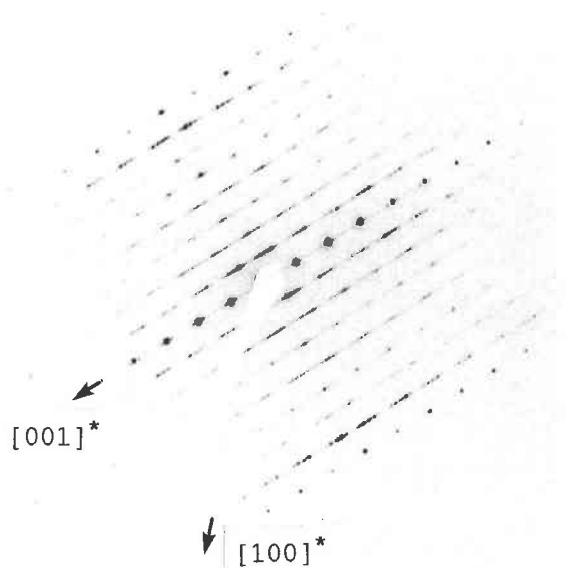


Fig. 4. The *h0l* net of parsettensite. This diffraction pattern comes from the area of the mineral grain that produced the image in Fig. 5. Note that $h = 2n$, in accord with a *C*-centered cell. This pattern is unusual in that the streaking is not complete, and the stacking disorder is only partial. The sample is from Gambatesa, Italy.

a pillar of less density. Each type of pillar on opposing sides of the rows of maxima are offset by shifts of $\pm a/3$.

Figure 5 shows an area of crystal that is periodic along *c* (lower portion), but with several stacking faults near the center and top portions of the figure (note curved arrows). Such faults are responsible for streaking between reflections from different twin components. Most crystals are highly disordered.

TRIAL-AND-ERROR PROCEDURES AND DATA PROCESSING OF TEM RESULTS

Initial model development

The distribution of the intensities that define the six-pointed star on the basal plane net (Fig. 2) probably represents a feature of the superlattice that is fundamental to the structure. Trial-and-error modeling indicates two possible island-shaped configurations that may generate six-pointed stars in a diffraction pattern: a three-pointed pinwheel pattern, which interacts with a center of symmetry to produce a six-pointed star, and a six-pointed star shape. The successful model was of the latter type.

The high-resolution image may be interpreted in a straightforward way, within the constraints of resolution. The row of elongated maxima along (001) represents the 2:1 layer. The 4.6-Å wide regions of high electron density (pillar) in the interlayer region conform to the expected width of two tetrahedra (projected O-O edge of 2.33 Å). Relative densities suggest approximately twice the number of projected tetrahedra in regions of higher density

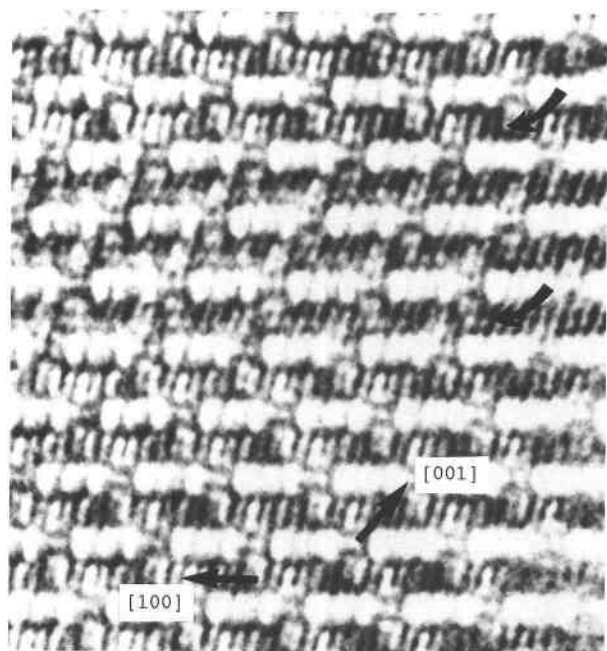


Fig. 5. High-resolution bright-field image from $h0l$ net of Fig. 4 taken by a JEOL 200CX. Arrows (right side of figure) show stacking errors.

relative to lower density regions. These relative densities are useful as a suggestion in developing trial-and-error models, but such models must conform to all the data presented, including the determined chemistry, unit-cell parameters, and X-ray data. Although many models were derived, only one model successfully accounted for all the data. This model (Fig. 6) is based on the stilpnomelane island but differs from the model stilpnomelane structure in the type of island connectors and the number of tetrahedra that point toward the octahedral sheet within the island.

Although a model that conforms to the data is an important first step, it is of significance to determine if the model uniquely satisfies the data, insofar as possible. A Fourier synthesis is a procedure that helps to do this, but obtaining the necessary intensity data from an electron diffraction experiment is often impossible because of dynamical diffraction effects. However, a kinematical approximation is approached in electron diffraction experiments under certain conditions: for very thin particles and where orientation effects are small. Parsettensite exhibits the latter condition because tilting experiments from (001) show that the intensities of the superstructure reflections are little affected over large tilts ($\pm 50^\circ$). Furthermore, because parsettensite has a perfect (001) cleavage similar to other phyllosilicates, applied stress produces extremely thin particles with parallel top and bottom grain boundaries. These conditions allow the use of kinematical approximations in calculations involving superstructure reflections measured at or near the basal plane [i.e.,

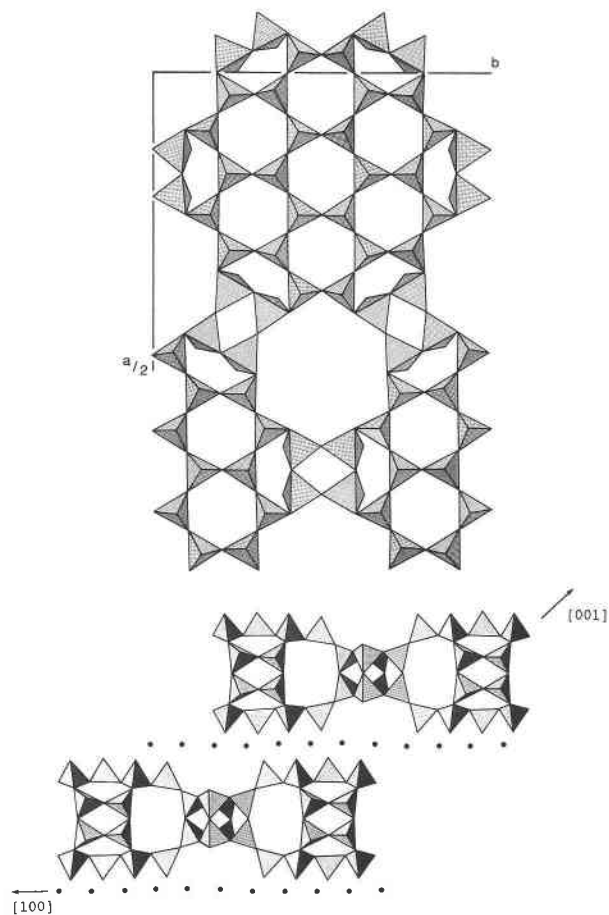


Fig. 6. The structure of parsettensite projected down c^* in top and projected down b in bottom. Solid circles represent Mn cations.

(001)]. Further justification and discussion for this are given below.

Fourier analysis and distance least-squares analysis

Exposures of the basal plane net from a grain-mount specimen were taken on the JEOL 100CX at stop intervals of $\sqrt{2}$, starting with 0.18 through 45 s, to produce a series. At the first appearance of a group of reflections on a photograph, each reflection intensity was judged visually on the basis of 1 to 10 without the preparation of an intensity scale. Only reflections in the gray range were measured on any negative because the film can quickly become saturated. Therefore, the darkest reflection in the gray range was judged as a 10, and only reflections between 10 and 100% of this intensity were considered within each negative. In order to compare photos, reflections were found on each negative that were about equal in intensity and could be considered a 10. In many cases, the same reflection can be observed in the gray range on more than one photograph, especially if films are examined by optical microscopy or with a jeweller's loop. Thus, several independent measurements can be made for the

same reflection. Because the Kodak electron image film (type SO-163) did not record reflections below a fixed threshold, data from different groups were combined on one scale on the basis of the time differences between photographs and the measurements of the same reflection from different negatives. It is clear that the intensity data should be considered rough estimations because of the procedures used.

Because the basal plane net exhibits hexagonal symmetry, one-quarter of the reflections of the orthohexagonal cell were independently measured to $h = 14$ and $k = 9$ and then averaged in accord with hexagonal symmetry. These values were then related back to the orthohexagonal cell to produce a total of 72 reflections, and all calculations were made in Cmm two-dimensional projections.

We argue that the thin crystal and the frequency of stacking errors eliminates the c -axis repeat of the superstructure. Thus, continuous hk rods are extended in reciprocal space and are visible as points upon intersection with the basal plane net. The loss of periodicity perpendicular to the basal plane suggests that the intensities of these reflections are determined by the Fourier transform of a single layer. Thus, the superstructure reflections of the basal plane net (perpendicular to $[103]$) may be alternatively indexed as the hk net (see above).

Octahedral sheet ions were not used initially in the model because it was assumed that they make negligible contributions to the superstructure reflections. Therefore, phases were calculated initially by using xy values for Si and O of the portions of the model (Fig. 6) that did not include the nature of the interlayer connectors, in order to determine if these connectors could be deduced from the Fourier. It became apparent, however, that the data were not of sufficient quality to drive the synthesis to produce atoms that were not given as input. Nevertheless, the procedure was useful to distinguish between models. For example, an alternative model, with hexagonal rings as interlayer connectors in the large holes in the tetrahedral sheet of Figure 6 instead of the fourfold connectors, did not generate the input atoms in the derived Fourier map. The final R value for this alternative model was 0.4, whereas the successful model had a value of 0.2. Figure 7 compares the weighted reciprocal lattice of the hk basal plane with the calculated pattern and Table 3¹ gives these data in numerical form. It is clear from the large differences in R value that the data are of sufficient quality to distinguish readily between reasonable models.

The model as derived by trial-and-error procedures did not include any xy information about the interlayer material. The electron density map, however, suggested additional scattering at the center of all the hexagonal six-

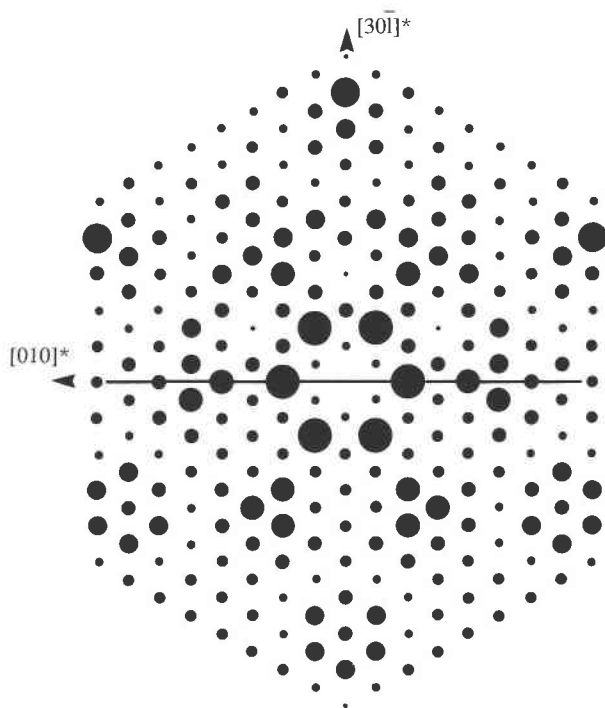


Fig. 7. A weighted electron diffraction pattern for the basal plane net of parsettenite showing calculated (top) and observed (bottom) reflections, using the model illustrated in Fig. 6. See text for details.

fold silicate rings, except the central ring of the island. The scattering (approximately 72 electrons) is consistent with the known presence of K, Ca, and H_2O . In addition, the Fourier analysis indicated that the tetrahedra of the four-membered ring connectors are tilted such that a tetrahedral edge is vertical.

The two-dimensional model can be easily transformed to a three-dimensional version on the basis of the layer-like qualities of the material. A DLS program (Baerlocher et al., 1978) was used. This approach only involves bond distances, unit-cell parameters, and space group, and the proposed topology as input. The procedure is useful only to confirm that the linkages are dimensionally reasonable. Input parameters included Mn-O distances (2.230 Å at 0.5 weight), T-O distances (1.625 Å at 1.0), O-O distances about the Mn (3.280 Å at 0.07), O-O distances about the T sites (2.655 Å at 0.07), and T-T distances (3.100 Å at 0.3) in space group $C2/m$. Because K is exchangeable and does not represent an integral part of the structure, no attempt was made to model its position. Because of the expected misfit between the tetrahedral and octahedral sheets, a small domed shape (± 0.2 Å) was imparted to the apical O plane associated with the Mn sheet, with the dome crest at the center of the islands. Besides parameters held invariant by special positions, all the z coordinates of these apical O atoms and O atoms at $z = 0.5$ were fixed for five cycles of refinement, after which only space group invariant coordinates and O z coordinates at

¹ A copy of Table 3 may be ordered as Document AM-94-552 from the Business Office, Mineralogical Society of America, 1130 Seventeenth Street NW, Suite 330, Washington, DC 20036, U.S.A. Please remit \$5.00 in advance for the microfiche.

TABLE 4. Derived atomic coordinates for parsettensite

Atom	x	y	z	Atom	x	y	z
Mn1	0.5743	0.0000	0.0087	O19	0.2219	0.1413	0.0919
Mn2	0.7186	0.0000	0.0133	O20	0.3621	0.1409	0.0859
Mn3	0.0000	0.0000	0.0000	O21	0.5056	0.1416	0.0926
Mn4	0.8578	0.0000	0.0016	O22	0.7248	0.2161	0.1025
Mn5	0.5000	0.0697	0.0000	O23	0.8638	0.2165	0.0917
Mn6	0.6475	0.0703	0.0139	O24	0.0078	0.2152	0.0964
Mn7	0.7880	0.0700	0.0075	O25	0.1518	0.2130	0.0999
Mn8	0.9282	0.0709	0.0000	O26	0.2946	0.2118	0.0960
Mn9	0.5744	0.1428	0.0079	O27	0.4344	0.2134	0.0910
Mn10	0.7173	0.1429	0.0091	O28	0.5799	0.2151	0.0997
Mn11	0.8571	0.1430	-0.0002	O29	0.5191	0.1046	0.2571
Mn12	0.0000	0.1436	0.0000	O30	0.5868	0.0923	0.2604
Mn13	0.5000	0.2135	0.0000	O31	0.6624	0.1081	0.2927
Mn14	0.6456	0.2135	0.0086	O32	0.4505	0.0998	0.2546
Mn15	0.7849	0.2150	-0.0003	O33	0.4196	0.2041	0.2563
Mn16	0.9280	0.2143	-0.0023	O34	0.5192	0.2974	0.2581
Si1	0.4725	0.0680	0.2156	O35	0.5000	0.3958	0.2964
Si2	0.5427	0.1343	0.2201	O36	0.4529	0.3058	0.2588
Si3	0.6139	0.0681	0.2284	O37	0.5570	0.2020	0.2600
Si4	0.4043	0.1366	0.2148	O38	0.5980	0.2976	0.2960
Si5	0.4056	0.2723	0.2191	O39	0.5032	0.5000	0.3542
Si6	0.4750	0.3381	0.2203	O40	0.4548	0.4134	0.3531
Si7	0.5436	0.2701	0.2216	O41	0.6603	0.2175	0.3403
Si8	0.5022	0.4316	0.3778	O42	0.4867	0.0000	0.2545
Si9	0.6946	0.1603	0.3800	O43	0.6341	0.0000	0.2647
Si10	0.6549	0.2779	0.3790	O44	0.6853	0.3303	0.3864
Si11	0.3366	0.0679	0.2156	O45	0.7245	0.1397	0.5000
Si12	0.2701	0.1369	0.2192	O46	0.6816	0.2668	0.5000
Si13	0.2030	0.0679	0.2218	O47	0.5500	0.4124	0.5000
Si14	0.3410	0.3428	0.2275	O48	0.3155	0.0993	0.2570
Si15	0.2738	0.2726	0.2275	O49	0.2497	0.1021	0.2597
Si16	0.4251	0.4293	0.3821	O50	0.1997	0.1007	0.2966
Si17	0.2236	0.1549	0.3798	O51	0.3827	0.1045	0.2546
Si18	0.2634	0.2723	0.3810	O52	0.3195	0.3109	0.2675
O1	0.6544	0.0000	0.1106	O53	0.3699	0.4030	0.2928
O2	0.7980	0.0000	0.1086	O54	0.3837	0.3008	0.2605
O3	0.9374	0.0000	0.0990	O55	0.2885	0.2040	0.2605
O4	0.0796	0.0000	0.0973	O56	0.2639	0.2949	0.2963
O5	0.2215	0.0000	0.0931	O57	0.4284	0.5000	0.3868
O6	0.3611	0.0000	0.0851	O58	0.2323	0.2119	0.3409
O7	0.5061	0.0000	0.0963	O59	0.3512	0.0000	0.2544
O8	0.7269	0.0723	0.1091	O60	0.2185	0.0000	0.2601
O9	0.8670	0.0718	0.0994	O61	0.2366	0.3248	0.3847
O10	0.0078	0.0718	0.0961	K1	0.0568	0.2000	0.4750
O11	0.1515	0.0712	0.0971	K2	0.1234	0.0000	0.4750
O12	0.2913	0.0706	0.0869	K3	0.2401	0.0000	0.4750
O13	0.4325	0.0710	0.0868	K4	0.1151	0.3750	0.4750
O14	0.5801	0.0718	0.1018	K5	0.9234	0.2000	0.4750
O15	0.6544	0.1429	0.1074	K6	0.8568	0.0000	0.4750
O16	0.7963	0.1439	0.1011	K7	0.7401	0.0000	0.4750
O17	0.9366	0.1433	0.0960	K8	0.8651	0.3750	0.4750
O18	0.0796	0.1419	0.0970				

Note: K coordinates are from Fourier analysis and were not included in the DLS refinement (see text).

$z = 0.5$ were fixed. This model assumes complete Al vs. Si disorder. Refinement converged in six additional cycles ($R = 0.006$), and atom positions are given in Table 4. The R factor does not give the correctness of the structure, but it does indicate that the proposed atom positions can be linked in accord with the topology of the model and separated by reasonable distances, as applied in the input.

Computing the electron optical image

The resulting atomic positions from the DLS refinement (Table 4) were used to calculate an electron optical image using program EMS (Stadelmann, 1987), which

uses the multislice method (Cowley and Moodie, 1957). Experimental conditions for the $h0l$ orientation were taken as $C_s = 1.2$ mm, half-angle of beam convergence of 0.0008 radians, half-width of focal spread of 90 Å, foil thickness of 68 Å (three unit cells along [010]), and an aperture diameter of 3.0 Å⁻¹. The slice thickness was 2.85 Å, and absorption was not considered.

Initial calculations included interlayer K, but images could only be matched to the observed patterns by removing exchangeable cations. This result is consistent with the SEM data that show high K mobility in the presence of an electron beam. It is noteworthy, however, that a focused beam in the SEM with a bulk (effectively infinitely thick) specimen involved K mobility toward the beam, whereas extremely thin specimens, which were derived from ion thinning, appear to involve K movement away from the beam in the TEM.

Several focal conditions were considered, and two sets of calculated and observed images are shown in Figure 8. Defocus conditions of -75 and -98 nm produced the best match between these calculated and observed images for the consecutive through-focus series involving the $h0l$ orientation. The calculated images were very sensitive to the focal condition, with differences of 2 nm making considerable changes in the apparent image. The aperture diameter of 3.0 Å⁻¹ used in Figure 8 is larger than the 2.0 Å⁻¹ aperture used experimentally to enhance the resolution of the calculated image, but all other parameters used in the calculated images match those of the microscope. A comparison of the observed and calculated images shows adequate agreement, when the differences in resolution are considered.

DISCUSSION

The kinematical approach: Further justification and implications

For an experiment at a given temperature, the strength of diffraction is dependent on the structure amplitude and scattering factor of the atoms, the direction of the incident beam, crystal thickness in the beam direction, the form and frequency of occurrence of deviations from crystal periodicity, absorption, and some inelastic scattering processes (e.g., see Cowley, 1981, chapters 8-11, 15). The structure amplitude and the scattering factor of the atoms are the required functions to describe a crystal structure. Thus, it is important to understand the effect of the other parameters on the intensity of diffraction.

For a crystal plate, tilting the specimen produces a controlled change in specimen thickness. Thus, the direction of the incident beam, crystal thickness, and absorption are being varied by a tilting experiment. For the most part, therefore, a tilting experiment provides a simple and rapid test to determine qualitatively the magnitude of dynamic diffraction effects. A thin crystal plate offers the best conditions for minimizing such effects.

According to Cowley (1988, p. 75), the kinematical approximation to electron diffraction intensities is reliable

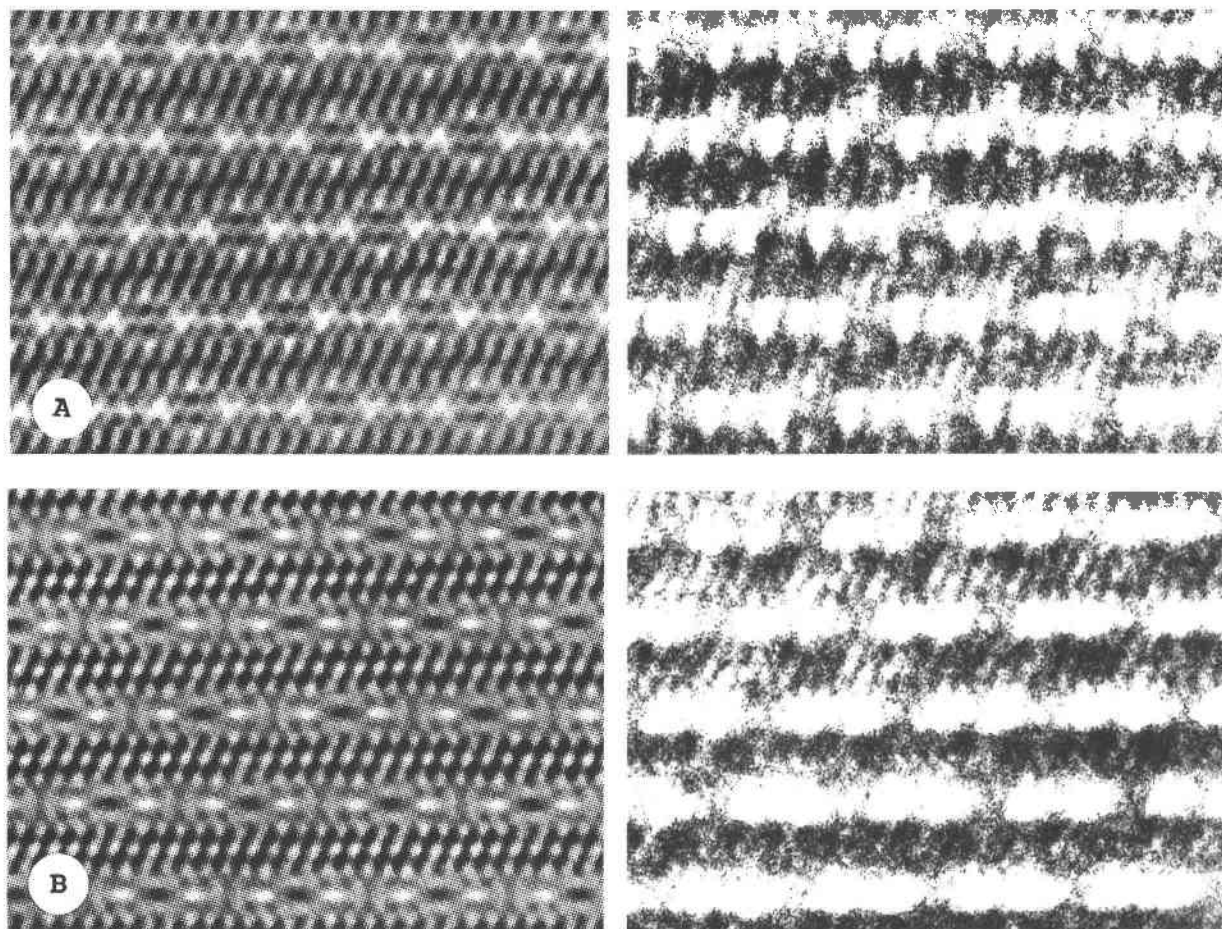


Fig. 8. Image calculations of parsettensite using the EMS program of Stadelmann (1987). Calculated $h0l$ images are shown on the left and are compared with actual images on the right. The image calculations do not include exchangeable cations, which probably have diffused out of the structure (see text). (A) Calculated at -75 nm; (B) calculated at -98 nm. The images on the right are from a consecutive through-focus series. Other conditions for the calculations are given in the text. Note that the calculated images have greater resolution than the observed images.

to within 10% for organic crystals up to about 100 \AA thick with 100 kV electrons, increasing to 200 \AA with 1 MeV electrons. He further noted that the kinematical approximation is more closely satisfied for large unit cells (as found in many organic crystals) and where there are many weak reflections, though he balances that by noting that the large number of reflections increases the possible contributions by double diffraction. Nonetheless, it is reasonable that a supercell produced by atoms of low atomic number (Si, O only, $Z = \sim 10$) and with many weak reflections, on a purely theoretical basis, should produce reflections based on kinematical approximations to within 10% for the thickness used here. This argument, combined with the observations that the reflections are certainly kinematic, since they do not vary with thickness and tilt, allows the use of Fourier analysis. Since a reasonable structural model has been derived, it is possible to calculate quantitatively the effect of thickness on the intensity of the diffracted beams. Figure 9 shows repre-

sentative results for calculated intensities for reflections used in the Fourier analysis. The figure uses intensities normalized to 1.0 over a thickness from 10 to 100 \AA . Because the intensities are based on a three-dimensional model and the observed data are based on a two-dimensional (disordered) structure, comparisons in intensity between reflections are not meaningful. However, the small changes in intensity for individual reflections vs. sample thickness are meaningful and indicate that dynamical effects were minimal.

For parsettensite, which has a perfect (001) cleavage, extremely thin particles with parallel top and bottom grain boundaries can be produced by abrading with a file; strain and defects are not introduced in the crystal structure. Furthermore, it is noteworthy that some reflections may be more affected than others by dynamical effects, and it becomes possible, therefore, to determine if a class of reflections within a diffraction plane, such as superstructure reflections, are relatively unaffected by dynamic dif-

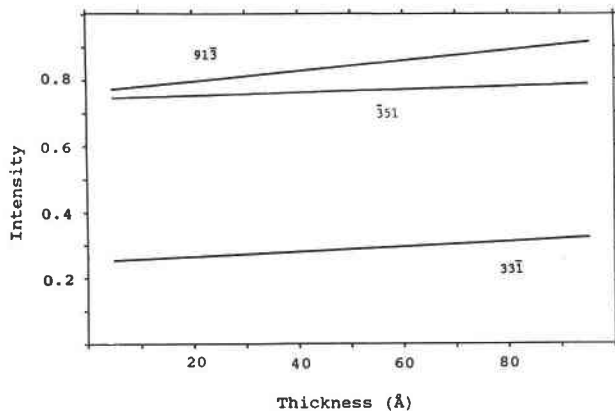


Fig. 9. Selected reflections used in the Fourier analysis showing the effect of intensity on the basis of unity vs. sample thickness, up to 100 Å.

fraction effects. The thinness of the sample and the large-scale stacking disorder produces diffraction rods along c that are uniformly streaked. This is experimentally shown by the observation that the intensities of the hk (superstructure) diffractions do not change over the tilting range. Thus, it is unnecessary to integrate over the length of the streaks, because they are invariant in intensity with tilt; it is sufficient to measure the intensity of the streak cross section, as done in this study.

Furthermore, as with the early work on X-ray diffraction patterns and structural determinations, the errors associated with the measured intensities can be fairly high (because of either rudimentary measurements or limited dynamical effects or both) and it is still possible to outline roughly the structure, such as is done here. Although not pursued here, the restriction that a crystal plate be used may not be mandatory, although it is advisable to proceed with caution. Also, the tilting test given above for dynamical effects does not necessarily require a $\pm 50^\circ$ tilt; a much smaller angular deviation before intensities vary significantly may indicate that thickness effects only become problematic above a critical point. Finally, because the magnitude of the dynamical effects varies for different crystallographic directions, reflections greatly affected by dynamical effects in one diffraction plane may be kinematical in others.

Structural formula

The ideal three-dimensional model can be used with the chemical data (Table 1) to determine a structural formula. With the assumption that all Mn is divalent, the formula is approximately $M_{7.5}^+(Mn, Mg)_{49}(Si_{64.5}, Al_{7.5})_{\Sigma=72}O_{168}(OH)_{50} \cdot nH_2O$, where M^+ is an exchangeable cation such as K, Na, or minor Ca. The substitution of trivalent Mn is possible, with the following exchange most plausible: $Mn^{2+} + H^+ = Mn^{3+}$. It is unknown if significant Mn^{3+} is present or, if present, whether it is primary or secondary. We believe, however, that Mn^{2+} is the predominant valence state present and that Al is essential to

the structure, in accord with the expected misfit between an ideal Mn-rich octahedral sheet and an attached tetrahedral sheet.

Comments on topology

The interisland linkages involve a double four-membered ring, which is a previously unknown linkage type in minerals but is similar to the geometry of the double four-membered ring in the synthetic zeolite-A structure (Gramlich and Meier, 1971). A four-membered unit single sheet consisting of four- and eight-membered rings occurs in apophyllite (Bartle and Pfeifer, 1976). Of course, the tilting of the tetrahedra within the double four-membered ring in parsettensite differs from that in zeolite-A because the double four-membered ring must maintain connectivity between adjacent island boundaries within a plane. The out-of-plane tilting of interisland tetrahedra may help stabilize the parsettensite structure because T-T distances may be maintained at 3.1 Å. Further comments on the parsettensite structure are given in a DLS study by Guggenheim and Eggleton (1994).

CONCLUSIONS

Microscopists generally view the intensity of the electron diffraction pattern as relatively worthless for a structural study because of dynamical scattering effects. A simple tilting experiment, however, can be used to determine where the intensity of diffraction is not greatly affected by dynamical effects. For these cases, a structural determination can proceed effectively by Fourier methods. Such procedures may be effective for many different classes of materials, but especially for layer materials with superstructure reflections produced by atoms low in atomic number.

We note that the derivation of the minnesotaite structure (Guggenheim and Eggleton, 1986) was based on the same premise: the diffraction pattern may be utilized in special cases for structural information. Although the earlier study did not apply numerical methods, electron diffraction patterns were used to develop trial-and-error models as here, followed by laser techniques to produce optical diffraction patterns based on the models. Both studies, however, were similar in that the diffraction patterns contained useful intensity information.

ACKNOWLEDGMENTS

We appreciate the efforts of the reviewers of this paper, H.R. Wenk, P. Heaney, G. Guthrie, and an anonymous reviewer, who had the fortitude to check the parsettensite coordinates for consistency. We thank C. Francis, Harvard University, for providing us with sample 92661 from Gambatesa, Italy, the U.S. National Museum (Smithsonian) for sample R4901, Parsettens Alps, Grisons, Switzerland, and C. Wenger, Schweizerische Geotechnische Kommission, for sample P24 from the Geiger collection. We gratefully acknowledge the Geochemistry Program and the U.S.-Australia Cooperative Science Program of the National Science Foundation for providing support under grant EAR-9003688, the Australian Research Council for support, and the University of Illinois at Chicago for providing a sabbatical leave for S.G.

REFERENCES CITED

- Baerlocher, C., Hepp, A., and Meier, W.M. (1978) DLS-76: A program for the simulation of crystal structures by geometric refinement. Institute of Crystallography and Petrography, ETH Zurich, Switzerland.
- Bartl, H., and Pfeifer, G. (1976) Neutronenbeugungsanalyse des Apophyllit $KCa_2(Si_4O_{10})_2(F/OH) \cdot 8H_2O$. Neues Jahrbuch für Mineralogie Monatshefte, 1976, 58–65.
- Cowley, J. (1981) Diffraction physics, 430 p. North-Holland, Amsterdam.
- (1988) Elastic scattering of electrons by crystals. In P. Buseck, J. Cowley, and L. Eyring, Eds., High-resolution transmission electron microscopy and associated techniques, p. 58–109. Oxford University Press, New York.
- Cowley, J.M., and Moodie, A.F. (1957) The scattering of electrons by thin crystals. I. A new theoretical approach. Acta Crystallographica, 10, 609–619.
- Drits, V. (1987) Electron diffraction and high-resolution electron microscopy of mineral structures, 304 p. Springer-Verlag, Berlin.
- Dunn, P.J., Peacor, D.R., and Simmons, W.B. (1984) Lennilapeite, the Mg-analog of stilpnomelane, and chemical data on other stilpnomelane species from Franklin, New Jersey. Canadian Mineralogist, 22, 259–263.
- Dunn, P.J., Peacor, D.R., and Su, S.-C. (1992) Franklinphillite, the manganese analog of stilpnomelane, from Franklin, New Jersey. Mineralogical Record, 23, 465–468.
- Eggleton, R.A. (1972) The crystal structure of stilpnomelane. II. The full cell. Mineralogical Magazine, 38, 693–711.
- Geiger, Th. (1948) Manganerze in den Radiolariten Graubündens. Beiträge zur Geologie der Schweiz, Geotechnische Serie, 27, 89 p.
- Gramlich, V., and Meier, W.M. (1971) The crystal structure of hydrated NaA: A detailed refinement of a pseudosymmetric zeolite structure. Zeitschrift für Kristallographie, 133, 134–149.
- Guggenheim, S. (1986) Modulated 2:1 layer silicates (abs.). International Mineralogical Association 14th General Meeting, Stanford University, 116–117.
- Guggenheim, S., and Eggleton, R.A. (1986) Structural modulations in iron-rich and magnesium-rich minnesotaite. Canadian Mineralogist, 24, 479–498.
- (1987) Modulated 2:1 layer silicates: Review, systematics, and predictions. American Mineralogist, 72, 724–738.
- (1988) Crystal chemistry, classification, and identification of modulated layer silicates. Mineralogical Society of America Reviews in Mineralogy, 19, 675–725.
- (1994) A comparison of the structures and geometric stabilities of stilpnomelane and parsettensite: A distance least-squares (DLS) study. American Mineralogist, 79, 438–442.
- Hutton, C.O. (1938) The stilpnomelane group of minerals. Mineralogical Magazine, 25, 172–206.
- Jakob, J. (1923) Vier Mangansilikate aus dem Val d'Err (Kt. Graubünden). Schweizerische mineralogische und petrographische Mitteilungen, 3, 227–237.
- (1933) Die Manganerzlagerstätten zwischen Val d'Err und Rofina (Oberhalbstein), ihre Begleitminerale und ihre Genesis. Schweizerische mineralogische und petrographische Mitteilungen, 13, 17–39.
- Müller, F.P. (1916) Über einige Mineralien aus den Manganerzlagerstätten des Oberhalbsteins (Graubünden, Schweiz.). Zentralblatt für Mineralogie, 457–459.
- Ozawa, T., Takahata, T., and Buseck, P.R. (1986) A hydrous manganese phyllosilicate with 12Å basal spacing (abs.). International Mineralogical Association 14th General Meeting, Stanford University, 194.
- Sameshima, T., and Kawachi, Y. (1991) Coombsite, Mn analogue of zussmanite, and associated Mn-silicates, parsettensite and caryopilite, from southeast Otago, New Zealand. New Zealand Journal of Geology and Geophysics, 34, 329–335.
- Stadelman, P.A. (1987) EMS: A software package for electron diffraction analysis and HREM image simulation in materials science. Ultramicroscopy, 21, 131–146.
- White, J.S. (1987) Neotocite from the Foote Mine, North Carolina. Mineralogical Record, 18, 133–134.

MANUSCRIPT RECEIVED AUGUST 14, 1992

MANUSCRIPT ACCEPTED JANUARY 7, 1994